Nuclear Engineering and Technology 56 (2024) 5028–5036

Contents lists available at ScienceDirect

Nuclear Engineering and Technology

journal homepage: www.elsevier.com/locate/net

Original Article

Microstructure response and sodium corrosion behavior of ferritic-martensitic steel after proton irradiation

Jeonghyeon Lee[a], Taeho Kim[b], Taeyong Kim[c], Ji Hyun Kim[c,*]

[a] Small Modular Reactor Development Team, HD Korea Shipbuilding & Offshore Engineering, 447 Bundangsuseo-ro, Bundang-gu, Seongnam-si, Gyeonggi-do, 13553, Republic of Korea
[b] Advanced Fuel Cycle Technology Division, Korea Atomic Energy Research Institute, 111, Daedeok-daero 989 Beon-gil, Yuseong-gu, Daejeon, 34057, Republic of Korea
[c] Department of Nuclear Engineering, Ulsan National Institute Science and Technology, 50, UNIST-gil, Eonyang-eup, Ulju-gun, Ulsan, 44919, Republic of Korea

ARTICLE INFO

Keywords:
Ferritic/martensitic steel
Weight loss
Precipitation
Sodium corrosion

ABSTRACT

In nuclear reactors, cladding materials are irradiated by neutrons as well as various types of ion beams that can induce radiation damage. Proton irradiation has been used for the past few decades to simulate neutron damage because protons have a higher scattering cross-section than fast neutrons and can effectively form displacements. This study is aimed at investigating the irradiation effects on the corrosion behavior of FMS. Non-irradiated and irradiated FMS materials were used for corrosion and dissolution experiments in a liquid sodium environment. It was observed that the irradiated materials exhibited worse corrosion and dissolution than the non-irradiated materials.

1. Introduction

Liquid metal fast reactors, such as sodium-cooled fast reactors (SFR) are considered promising options for 4th-generation nuclear energy systems. Among the various liquid metal coolant materials under extensive research, sodium and lead-bismuth eutectic (LBE) have carried out experiment significant attention. The sodium possess unique characteristics as liquid metal coolants [1–3]. Liquid metal induces corrosion in materials, leading to dissolution of steel constituents such as nickel and chromium. Additionally, sodium offers benefits in terms of a large temperature difference between its melting and boiling points, which can be advantageous in terms of preventing pipe blockages and from a thermohydraulic perspective. Sodium is a highly effective heat transfer medium. The reactor core temperature ranges from 380 °C. to 600 °C which temperature has low dissolved oxygen concentration in the coolant. Although sodium has a reasonably low melting temperature, its low boiling point (883 °C) raises safety concerns related to coolant heat up during unprotected transients. Typical sodium velocities, in contrast, can reach up to 8–10 m/s, resulting in higher linear power being available and requiring a lower pitch-to-diameter ratio [4,5].

A wide range of engineering materials have been identified as being compatible with liquid alkali metals such as sodium, including stainless steels and low-carbon steels [6]. Among these materials, ferritic/martensitic steels (FMS) are particularly attractive for use as cladding and ducts in sodium-cooled fast reactors due to their high strength at high temperatures and good swelling resistance under irradiation. However, the effect of sodium on the mechanical strength of steel is constrained by three factors.

1. Corrosion and mass transfer,
2. Decarburization and carburization, and
3. Non-oxidation (reducing atmosphere) by sodium.

The mechanical strength of steels in a liquid metal environment is influenced by corrosion and leaching. In a high-temperature liquid metal environment, both ferritic and austenitic steel claddings undergo thickness reduction as a results of internal oxidation phenomena. It is worth noting that materials with higher carbon content exhibit a decarburization effect, leading to a more pronounced decrease in strength [7].

The corrosion behavior of FMS such as Gr. 92 and HT9 in oxygen-saturated liquid sodium at temperature of 650 °C and 550 °C was investigated by Shin et al. [8]. The study found that the corrosion of ferritic steels in high-temperature liquid sodium leads to the formation of Na-Cr-O compounds on the surface. These compounds can potentially influence the performance and efficiency of cladding materials.

---

* Corresponding author.
E-mail address: kimjh@unist.ac.kr (J.H. Kim).

https://doi.org/10.1016/j.net.2024.07.011
Received 5 November 2023; Received in revised form 3 July 2024; Accepted 3 July 2024

The influence of irradiation on corrosion behavior has been widely reported [9,10]. Previous studies have investigated the irradiation assisted stress corrosion cracking in various environments and performed studies on crack formation in different reactor types by experimenting with various materials [11,12]. Based on previous research, it has been confirmed that irradiation effects are influenced by radiation-induced threshold chromium depletion, radiation hardening, localized deformation, selective internal oxidation, and irradiation creep [13,14].

Also, chromium leaching and precipitation can also in liquid metal environments, resulting in decreased strength and potential damage to the material [15]. While chromium is typically distributed within grain boundaries, its local depletion can occur in the vicinity of boundaries due to the formation of chromium compounds and oxides, thereby leading to localized deterioration and embrittlement of materials. In stainless steels, chromium depletion is widely recognized as a primary factor contributing to irradiation assisted stress corrosion cracking.

In particular, the irradiation environment can cause radiation-induced segregation of Cr, which can further accelerate chromium depletion. In addition, irradiation hardening that occurs with chromium precipitation can affect the strength of the material [16,17]. This study was undertaken to enhance our comprehensive of the consequences effects between irradiation damage and liquid metal corrosion in ferritic/martensitic steels. The primary objective of this investigation is to ascertain the effect of irradiation conditions on the corrosion rate of these steels, with potential implications for the performance and durability of cladding materials and other components employed in sodium-cooled fast reactors.

2. Experimental

2.1. Materials and specimen preparation

The chemical composition of the specimens used in this experiment is shown in Table 1. This composition was measured by glow discharge optical emission spectroscopy (GD-OES). Materials used in the experiment were normalized and tempered grade 92 steel (Gr. 92), which is an ASTM A182 material, and HT9 steel, which is commonly used as a nuclear material. The specimens were subjected to a normalization process at 1080 °C for 60 min, followed by tempering at 800 °C for 6 min to attain a martensitic structure [18]. Prior to proton irradiation, polishing was carried out sequentially using SiC grids of 320, 400, 800, and 1600, followed by a pretreatment utilizing diamond paste. And then the final polish was then applied using a gamma alumina (0.05 μm size) polishing.

2.2. Proton irradiation

To replicate the irradiated nuclear fuel cladding examined in this study, proton-irradiated FMS were used. To conduct the proton irradiation experiments, specimens were subjected to a 3 MeV proton beam at a dose rate of 1.2×10^{-6} displacement per atoms/s at the Korea Multipurpose Accelerator Complex (KOMAC) of the Korea Atomic Energy Research Institute. Total irradiation fluence is 0.5×10^{16} protons/cm^2 and 1×10^{16} protons/cm^2. And both terms will be used interchangeably in the subsequent content. The irradiation temperature of the specimens was closely monitored and maintained at 380 ± 5 K throughout the experiment and irradiation were conducted in an atmospheric pressure environment. The irradiated specimens, after undergoing a stabilization period of approximately three months following irradiation, were received and utilized in the experiments. The irradiated surface area was measured approximately to be 50 mm^2.

Table 1
Chemical composition of the specimens (wt.%).

	C	Si	Mn	Cr	Ni	Mo	W	V
Gr. 92	0.08	0.20	0.42	8.71	0.10	0.35	1.60	0.17
HT9	0.20	0.15	0.48	12.03	0.45	0.50	1.58	0.21

The ion irradiation experiment was designed using the Stopping and Range of Ions in Matter (SRIM) code [19,20]. Additionally, Norget-Robinson-Torrens (NRT) equation was utilized to estimate the accumulated irradiation damage caused by proton-irradiation in terms of dpa [21,22],

$$\mathrm{dpa} = \frac{0.8}{2E_d}\left(\frac{dE}{dx}\right)_n \frac{\varnothing_t}{\rho} \tag{1}$$

where E_d is the displacement energy, $\frac{dE}{dxn}$ is the linear energy transfer (LET) per ion to target by nuclear processes, $\varnothing_t$ is the fluence per unit area, and ρ is the atomic density of each specimen. These terms were obtained from SRIM by summing up phonon and binding energy profiles. The 3 MeV proton beams normal to Fe-12%Cr and Fe-9%Cr produce relatively uniform damage profiles between 1 μm and 30 μm, with damage peaks occurring at approximately 38 μm. This depth range is apt for the sodium corrosion test (shown in Fig. 1).

After the irradiation experiment, the specimen was subjected to examination using a scanning probe microscope in atomic force microscopy (AFM) mode with the semi-contact technique. The surface morphology and roughness of the FM steel were investigated using AFM (Bruker Corporation, Multimode V) after proton irradiation with varying fluences. Multiple AFM scans were conducted on a 10 μm x10 μm area for each condition of the specimen. Morphology images were obtained with a force constant of approximately 0.4 N/m. The surface roughness was quantified using the root mean square (rms) roughness, which was determined through 3D imaging using AFM software. To eliminate features such as surface noise and undulations, a combination of a first-order least square method and Gaussian filter was applied. This approach enbled the calculation of the precise rms value of the surface.

$$R_q = \sqrt{\frac{1}{N}\sum_{i=1}^{N} y_i^2} \tag{2}$$

where N is the number of intervals across the interface and y is the interface height at a given point.

Ex situ investigations were conducted to characterize the precipitate utilizing various techniques, including scanning electron microscopy (SEM), energy-dispersive X-ray spectroscopy (EDS), and transmission

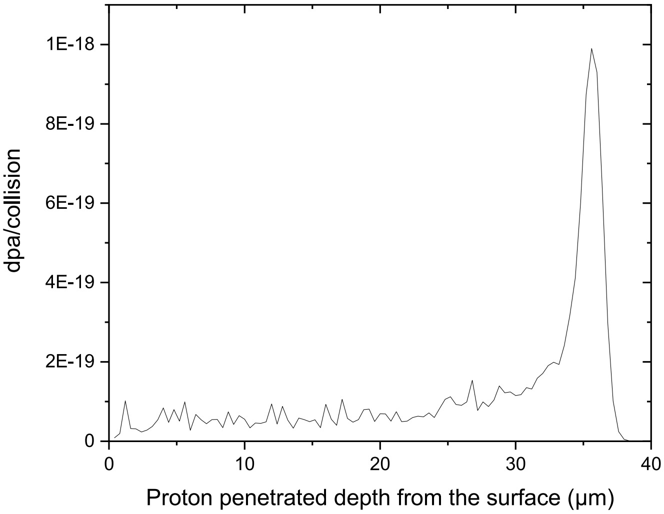

Fig. 1. The calculated damage profile (Stopping and Range of Ions in Matter) in Gr. 92 irradiated with 3 MeV protons. The damage peak occurs around 38 μm into the sample and uniform damage occurs between 1 μm and 30 μm.

electron microscopy (TEM). For TEM analysis, the samples were prepared using the focused ion beam (FIB) milling method. To prevent surface contamination from impurities and minimize ion beam-induced damage during the FIB process, a carbon coating was applied to the specimen surface. The samples were then precisely cut and thinned utilizing gallium ions. The FIB samples were meticulously prepared using a Quanta 3D FEG dual-beam FIB instrument.

2.3. Micro hardness measurement

To measure the microhardness at room temperature, the Vickers hardness was determined using a diamond indenter. A load of 1 kgf was applied to the specimen to measure the hardness, and five points were measured on each specimen to obtain an average value and evaluate the level of error. The hardness was calculated using the following equation,

$$HV = \frac{F}{A} = \frac{1.8544F}{d^2}\left[\frac{\text{kgf}}{\text{mm}^2}\right] \tag{3}$$

where F represents the applied load in kgf. A represents the cross-sectional area, and d represents the length of the cross-section, expressed in mm.

2.4. Corrosion test

To maintain the saturation of dissolved oxygen in sodium, a gas mixture of oxygen and helium was bubbled into the autoclave containing sodium, which was located within an environmentally controlled glove box. The autoclave was fabricated using 316L stainless steel, while an alumina crucible container was utilized to restrict contact between sodium and the 316L autoclave. The experimental temperature was maintained at 650 °C throughout the 300-h duration. Temperature control was achieved using a PID system coupled with a K-type thermocouple immersed in the sodium-filled container weighing 0.8 kg. The specimens were exposed to the sodium environment for 300 h, respectively, in order to accelerate oxidation under the corrosive environment by utilizing oxygen-saturated sodium [23,24].

3. Results

3.1. Irradiation effect on FMS

In Fig. 2 shows AFM morphology depicting the varied morphologies observed after the irradiation experiment on the Gr. 92 specimen. The AFM images depict the surface morphology of the specimens before and after proton irradiation. As observed in the figures, the surface protrusions and the rms roughness of the specimens increased due to the formation of precipitates after irradiation. Indeed, an increase in rms roughness was observed with an increase in irradiation fluence, indicating a rougher surface. These observations align with the results obtained from SEM images and TEM analysis. Ion irradiation not only increases surface roughness by causing collisions with the metal surface but also promotes the formation of precipitates, which further alters the surface roughness. As a result, the effective surface area increases, potentially influencing corrosion behavior. Moreover, ion irradiation can act as a contributing factor in increasing the pathways for oxygen penetration.

The investigation experiments were performed using a proton beam source with an energy of 3 MeV, and the surface analysis results can be seen from Fig. 2. The rms of surface roughness values for unirradiated, 5 × 10^{15} protons/cm^2 irradiated, and 10^{16} protons/cm^2 irradiated specimens were determined to be 1.51 nm, 5.84 nm, and 8.14 nm, indicating an overall increase in surface roughness. The three-dimensional visualization allowed for the observation of surface roughness changes. As mentioned earlier, it appears that the increased formation of precipitates had a significant impact on the surface roughness. However, it is important to note that the doubling or quintupling of the rms values does not necessarily imply a proportional increase in the corrosion rate. It is necessary to differentiate and understand these factors accordingly.

The SEM images and TEM images are discussed to investigate the irradiation effect on precipitate formation in Gr. 92 (Figs. 3 and 4). From

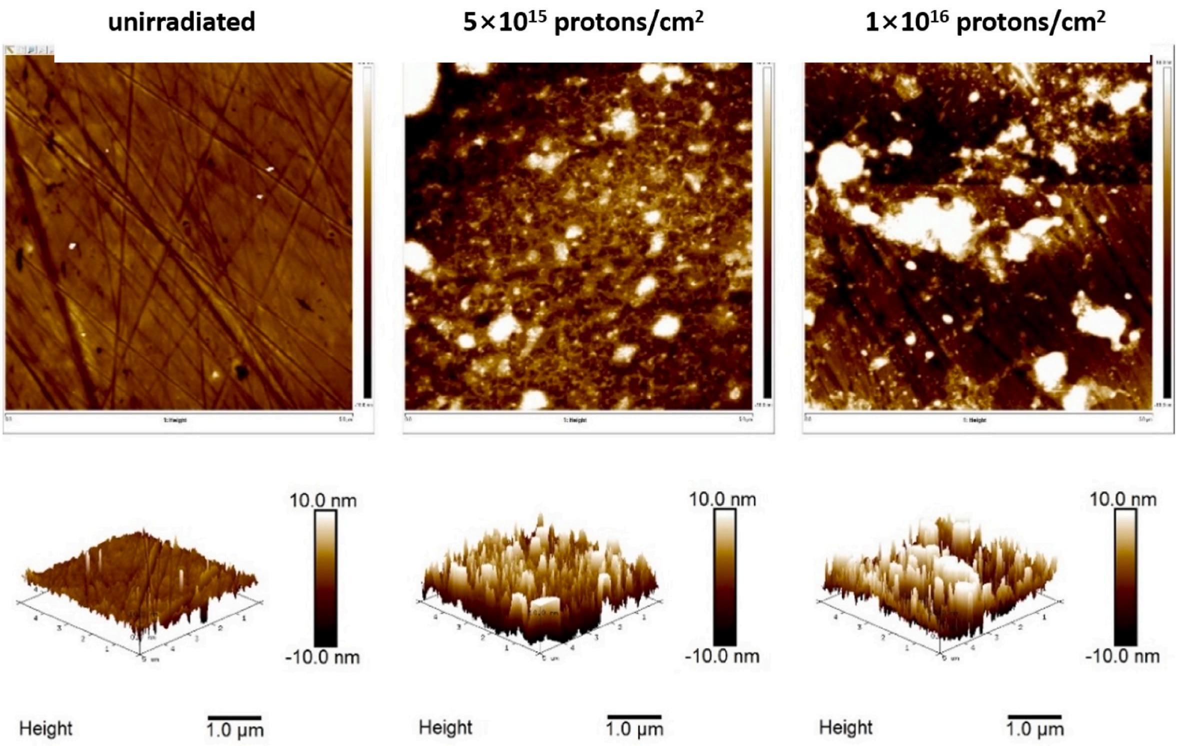

Fig. 2. Atomic force microscopy image of the surface of (a) unirradiated Gr.92 specimen, (b) 5 × 10^{15} protons/cm^2 irradiated Gr.92 specimen, and (c) 10^{16} protons/cm^2 irradiated Gr. 92 specimen.

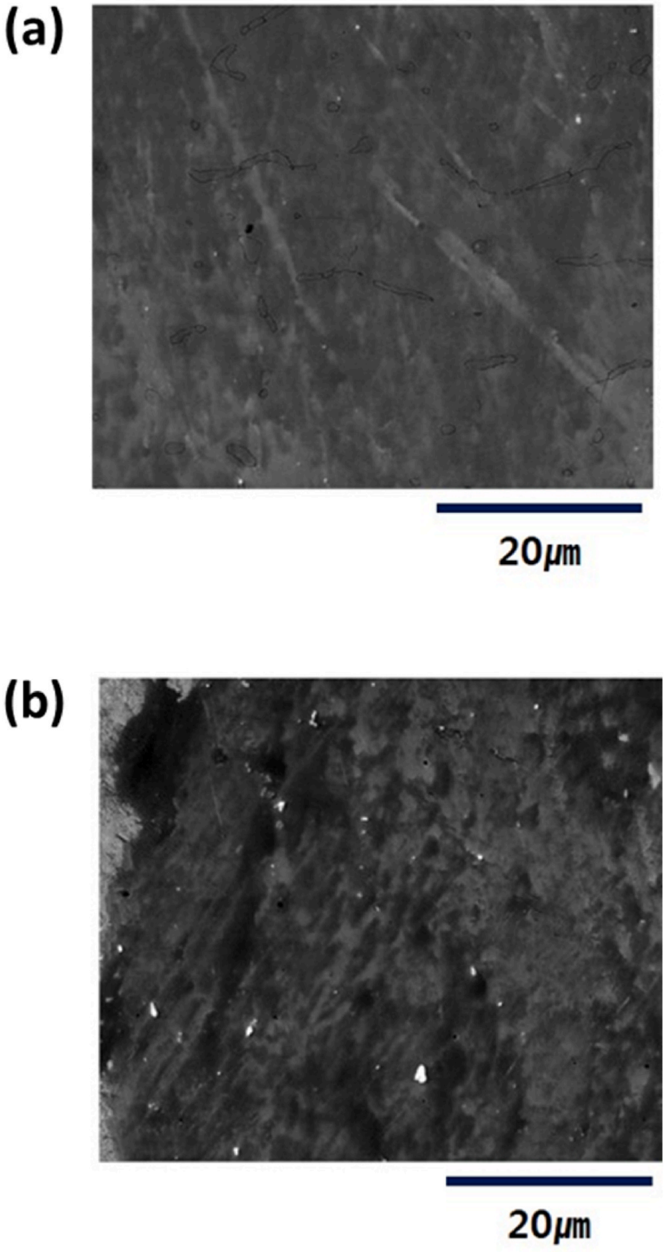

Fig. 3. Secondary electron images of (a) unirradiated Gr.92 specimen, and (b) 10^{16} protons/cm^2 irradiated Gr. 92 specimen.

the TEM analysis, it is observed that chromium precipitates known as $M_{23}C_6$ (M; Fe, Cr, W, mainly Cr) were formed and coarsened with the irradiation of the specimen, which is similar to the trend observed in the results of the SEM-EDS analysis. According to Jiao and He et al. $M_{23}C_6$ precipitates increase when exposed to irradiation [25–27]. Coarser precipitates were observed along prior austenite grain boundaries and along sub-grain boundaries, examined using atom probe tomography. Hence, the increase in carbon and chrome concentrations might be the reason for the slight coarsening of the precipitation under the effect of diffusion enhanced by proton irradiation.

The EDS results in Fig. 4 confirmed that the precipitates were identified as $M_{23}C_6$ carbides, which was further supported by the matching diffraction patterns analyzed in Fig. 5. The *d-spacing* at position A was explained using JCPDS reference data for diffraction analysis (14–0407, 003–1176, 003–1172; $Cr_{23}C_6$). Additionally, Fig. 5 clearly demonstrated the increased presence of $M_{23}C_6$ carbides after proton irradiation.

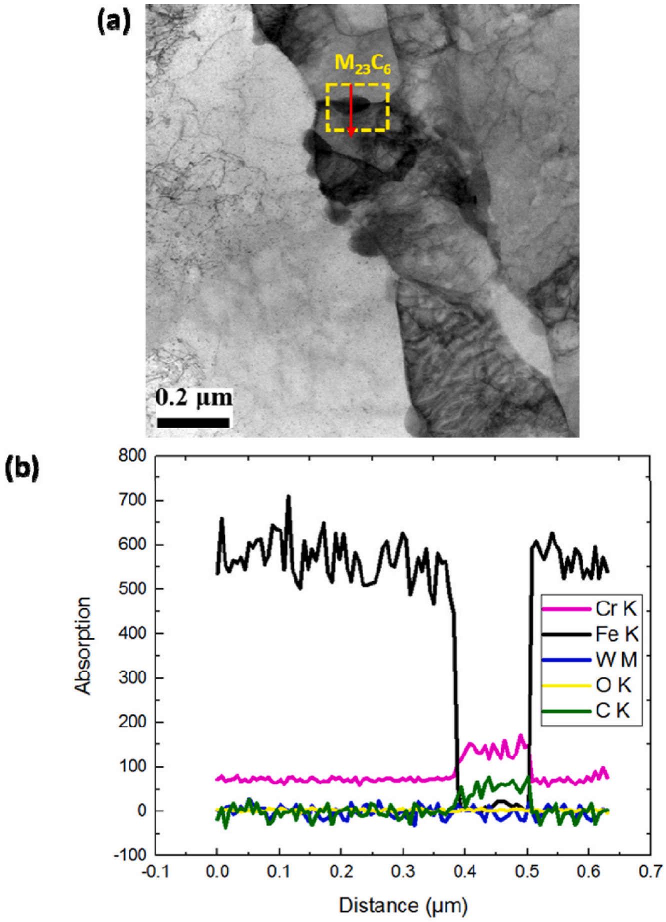

Fig. 4. Bright-field transmission electron microscopy image and EDS analysis results of cross-section of 10^{16} protons/cm^2 irradiated Gr. 92 specimen under irradiation.

3.2. Irradiation damage in the absence of dislocations

The density of dislocation loops increased between unirradiated environment and 5 × 10^{15} protons/cm^2 irradiated, and 10^{16} protons/cm^2 irradiated for the Gr. 92 specimen. TEM measurements of the irradiated specimens were performed at various magnifications to confirm the presence of dislocation loops in the specimens. Dislocation loop size and number generally increased with increasing dose. Fig. 6 shows dislocation loops in the specimen.

Numerous investigations, including those conducted on diverse steels like austenitic steel and ferritic/martensitic steel under various ion irradiation conditions, suggest that proton irradiation, similar to neutron irradiation, primarily induces the formation of dislocations and dislocation loops within steels. Dislocation channels serve as pathways for dislocation slip. However, the dislocations and dislocation loops largely constrained within the channels due to the presence of a harder matrix, resulting in the generation of larger slip steps.

3.3. Corrosion behavior of irradiated FMS

To evaluate the impact of irradiation, a corrosion experiment was conducted by immersing the samples to a high-temperature liquid sodium environment at 650 °C for a duration of 300 h. Subsequently, the weight change resulting from metal loss and the formation of reaction layers on the specimens were quantified [1,28,29].

Fig. 7 shows the FIB images of both unirradiated and irradiated Gr. 92 specimens. In the images, dark regions represent chromium-rich zones, which measure approximately 9.98 μm, 11.64 μm, and 12.32

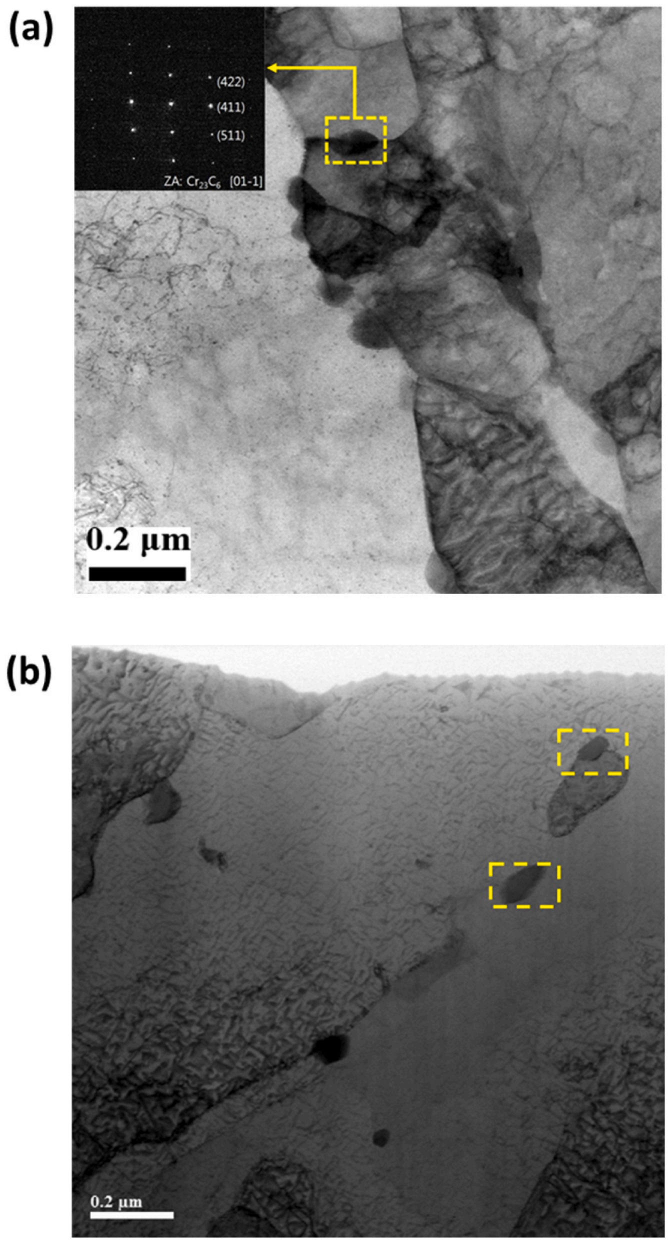

Fig. 5. (a) Bright-field transmission electron microscope image of 10^{16} protons/cm^2 irradiated Gr. 92 specimen. The diffraction pattern was analyzed at the region marked with yellow box and the result showed in inset. The diffraction patterns clearly show that has d-spacing of $Cr_{23}C_6$, (b) $M_{23}C_6$ carbides at the un irradiated specimen. (For interpretation of the references to colour in this figure legend, the reader is referred to the Web version of this article.)

µm in thickness for the unirradiated, 5×10^{15} protons/cm^2 and 1×10^{16} protons/cm^2, respectively. The chromium-rich zones on the irradiated specimen are thicker compared to those on the unirradiated specimen, primarily due to an extended corrosion path. EDS analysis findings presented in Fig. 8 indicate the presence of sodium chromite oxide. Moreover, the line profiling results in Fig. 7 demonstrate the formation of a chromium-rich phase known as $NaCrO_2$. These outcomes provide evidence that sodium and oxygen are the driving factors behind the development of the chromium-rich zones [23,30].

The presence of oxygen in liquid sodium manifests in the form of Na_2O. The formation of sodium chromite occurs through the reaction described in Equation (4). Chromium, being a highly reactive element with strong oxide-forming characteristics, readily interacts with the Na_2O dissolved in sodium, resulting in the formation of $NaCrO_2$, as depicted in Equation (5). NaCrO $^{+}$ exhibits greater stability in liquid sodium compared to Na_2O.

$$2\mathrm{Na}(\mathrm{l}) + \frac{1}{2}O_2 \rightarrow Na_2O(s) \tag{4}$$

$$2\mathrm{Na}_2O(soln.) + Cr(s) \rightarrow NaCrO_2 + 3Na(l) \tag{5}$$

In order to explain the presence of $NaCrO_2$ in FMS specimens, Energy-Dispersive X-ray Spectroscopy (EDS) analysis was conducted along with X-ray profiling analysis. The EDS analysis confirmed the formation of sodium-chromium-oxygen compounds on the specimen surface, with detected peaks corresponding to oxygen, sodium, and chromium at precise locations. Subsequently, X-ray Photoelectron Spectroscopy (XPS) analysis was performed on the specimens exposed to 650 °C oxygen-saturated sodium for 300 h, including measurements, C 1s, O 1s, Na 1s, and Cr 2p spectra. The XPS spectra obtained from Fig. 9 confirmed the presence of $NaCrO_2$ compound on the specimen surface. Remarkably, the $NaCrO_2$ compound was found to be attached to the specimen surface. Furthermore, individual spectra for sodium, chromium, carbon, and oxygen were obtained to investigate the possibility of compound formation through the reaction between the specimens and high-temperature sodium.

The weight change of the specimens were measured after exposure to high-temperature liquid sodium for 300 h. Three specimens were used, and measurements were conducted three times for each specimen to obtain an average value for evaluation. The findings, including the corrosion rate of chromium content and radiation damage amount, are summarized in Table 2. The results reveal that the irradiated specimens exhibit more weight loss than the unirradiated specimens. Additionally, the Gr. 92 specimen demonstrates a more significant weight loss than the HT9 specimen, which may be attributed to the disparity in chromium content.

4. Discussion

Proton irradiation offers advantages over electron, heavy ion, and neutron irradiation, addressing their respective limitations. When operated at low energy (1–10 MeV), protons can achieve a penetration depth exceeding 100 µm, and the resulting damage profile exhibits a relatively flat distribution compared to other ions and electrons, resulting in dose rate variations of only a few tens of µm. Hence, proton irradiation provides an ideal experimental approach to investigate the combined effects of irradiation and liquid metal corrosion on FMS. The high-temperature liquid sodium induces material dissolution and oxidation, and it reacts chemically with the elements present within the material, leading to the formation of precipitates. These effects accelerate the corrosion process [23].

4.1. *Effect of irradiation on surface morphology of FMS*

The irradiation variables on surface and subsurface changes in materials can determine the individual processes such as corrosion behavior or diffusion transition by the change path. Proton irradiation produces isolated point defects and small widely spaced cascades, which are caused by coulomb interaction.

Proton irradiation damage in materials arises from collisions with nuclides, and then the reactions produce vacancy and interstitial atom. Interaction of radiation protons with a crystal lattice gives rise to defects or imperfections such as vacancies, interstitial atoms, ionization and electron excitation of lattice atoms. Those defects can produce irradiation damage to the material, which can influence the roughness and morphology at the surface of the specimen and displaced atoms in the material.

Corrosion rate is highly related to the surface condition of the specimen. From the roughness measurement, high radiation damaged

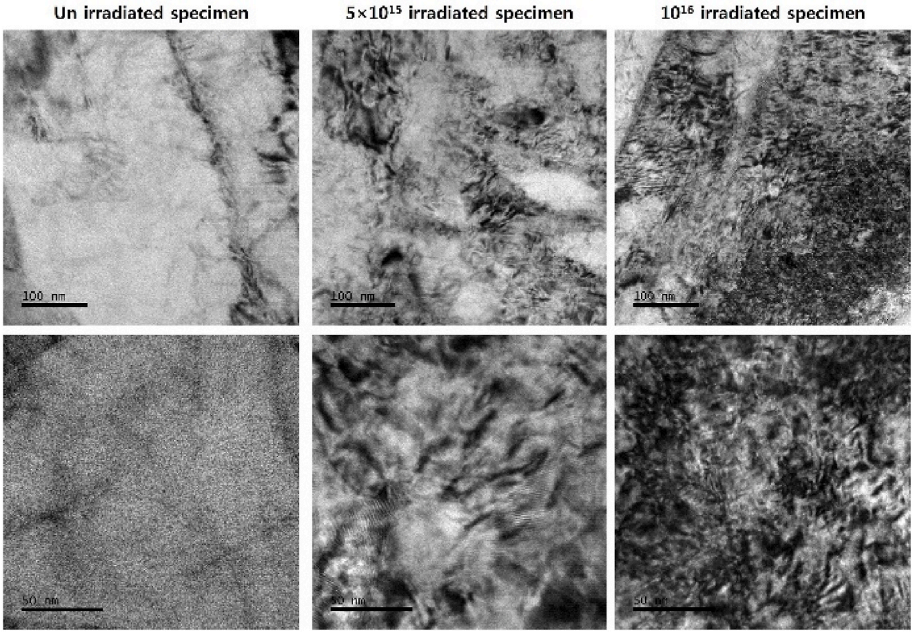

Fig. 6. TEM images of unirradiated Gr.92 specimen and irradiated Gr.92 specimen defects such as dislocation observed at 5 × 10^{15} protons/cm^2 and 1 × 10^{16} protons/cm.^{2}.

FMS have higher roughness than low radiation damaged FMS and unirradiated FMS. Typically, surface roughness influences corrosion, as an increase in the surface area in contact with a material allows for a broader active site for reactions. Consequently, in this study, where specimen surface roughness varies due to irradiation, the corrosion behavior of irradiated specimens is expected to differ from that of unirradiated specimens. This variance is attributed to the enhanced active surface area, which facilitates greater interaction with corrosive elements, potentially leading to accelerated corrosion processes. According to previous literatures, the variation in surface roughness of the tested specimens has an influence on pitting corrosion [6,7]. As observed in previous studies, a smoother surface of the specimens reduced the incidence of pitting corrosion, indicating the effect of surface roughness on pitting corrosion in stainless steel. Therefore, in this experiment, it is anticipated that surface roughness also contributes as one of the factors accelerating corrosion [31–34].

4.2. Effect of chromium precipitation on corrosion characteristics of FMS

Irradiation can trigger the formation of precipitates in materials, leading to radiation-induced segregation and precipitation. These phenomena are significant concerns in structural materials exposed to irradiating environments. Alterations in the composition of grain boundaries can create an unstable environment through modifications in microstructure and susceptibility to various processes. According to Gupta et al. the behavior of chromium in chromium alloys containing 9–12 wt% chromium content can induce the formation of chromium-rich phases, which can lead to the possibility of chromium depletion at grain boundaries [35].

The precipitation of $M_{23}C_6$ carbides along the grain boundaries and the subsequent depletion of chromium in these regions can induce sensitization of the material, leading to potential strength reduction and degradation. Previous studies have reported that irradiation of FMS results in chromium depletion along grain boundaries at different irradiation doses [17]. Under irradiation, precipitate phases, such as $Cr_{23}C_6$, undergo growth in size, changes in number density, and composition. Irradiation is known to be possible to accelerate the formation of chromium-rich precipitates through radiation-enhanced diffusion, radiation-induced precipitation and radiation-back diffusion [25–27, 36]. In steels, radiation-induced segmentation is a phenomenon in which interstitial atoms preferentially migrate to sinks under irradiation, reading to chromium depletion in the vicinity of the sink. Classical radiation-induced precipitation theories [21,37] can be used to explain the observed $Cr_{23}C_6$ precipitation in this study. The ion irradiation can induce the formation of chromium-rich precipitates in Fe-Cr alloy, which can have an impact on the material properties.

4.3. Chromium effect on corrosion

According to Shin et al., 9 wt% Cr steel and 12 wt% Cr steel show similar corrosion behavior. However, the corrosion rates of Cr steels differ. 9 wt% Cr steel has a higher corrosion rate than 12 wt% Cr steel in a high temperature sodium environment [28]. Chromium content has been widely known to resist corrosion. In addition, it is used as a corrosion resistant elemental material in various industries and research fields. The effects of chromium content on the weight loss behavior of ferritic stainless steel concluded that the material containing higher chromium content has less corrosion behavior than the material containing lower chromium content. The reason is that the extent of dissolution into the liquid metal is influenced by the composition of chromium in the base material [38]. A previous study showed that metal loss and weight change behaviors of ferritic stainless steel are continuously affected when the chromium content increases from 5 wt% to 15 wt% [39]. Further, $M_{23}C_6$ precipitates were formed more than unirradiated materials, causing local depletion of chromium. The chromium content is the major parameter for the corrosion resistance of stainless steels; the local decrease of chromium allows pre-irradiated corrosion along the grain boundaries. In irradiating environments, Cr-rich phases and precipitates have been reported in FMS; the authors suggested that those could provide sites for chromium segregation and play an important role in the materials [40–42].

Considering the presence of iron, nickel, and chromium atoms in the liquid metal corrosion system, the observed outcomes align with the known diffusivity characteristics of these solutes within iron, nickel, and chromium. Notably, nickel exhibits slower diffusion, chromium displays faster diffusion, and iron falls somewhere in between. Consequently, chromium depletion occurs at grain boundaries as the initial phenomenon. This process significantly influences the corrosion behavior of

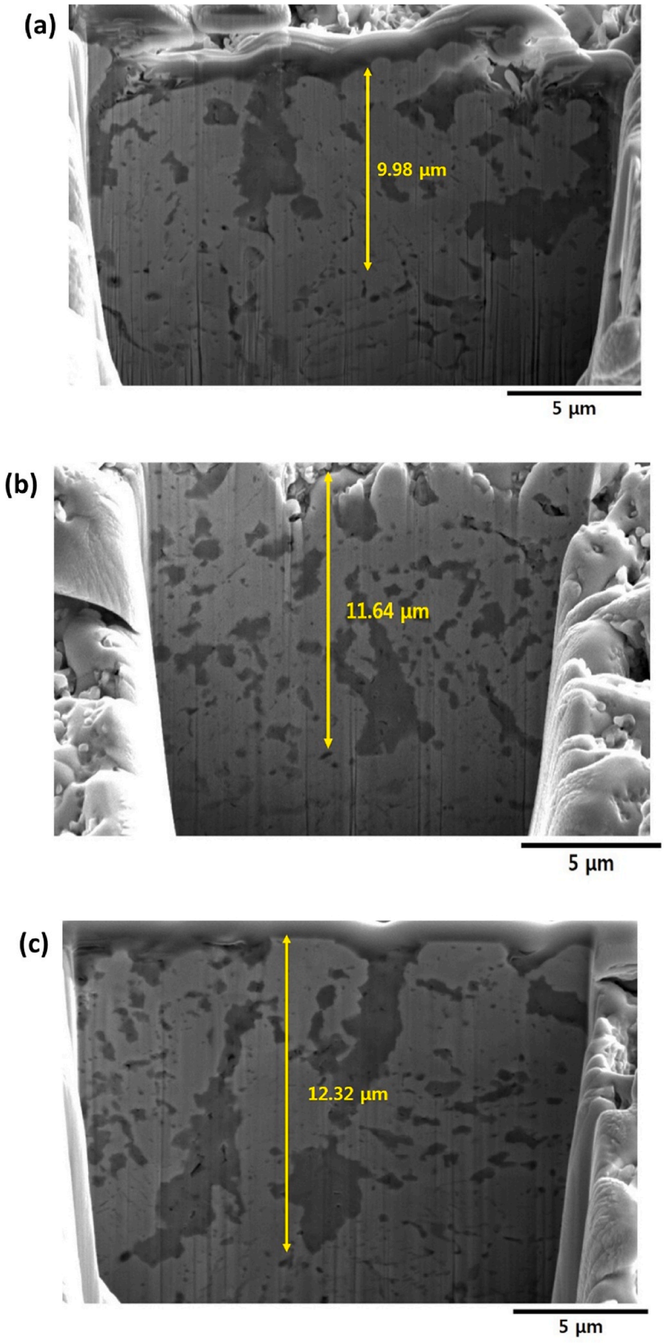

Fig. 7. FIB-SEM images of (a) unirradiated, (b) 5×10^{15} protons/cm^2, and (c) 1×10^{16} protons/cm^2 irradiated Gr. 92 specimen after 300 h exposure in 650 °C oxygen-saturated sodium. The vertical arrow bars indicate the depth of the chromium-rich zone from the surface of the metal.

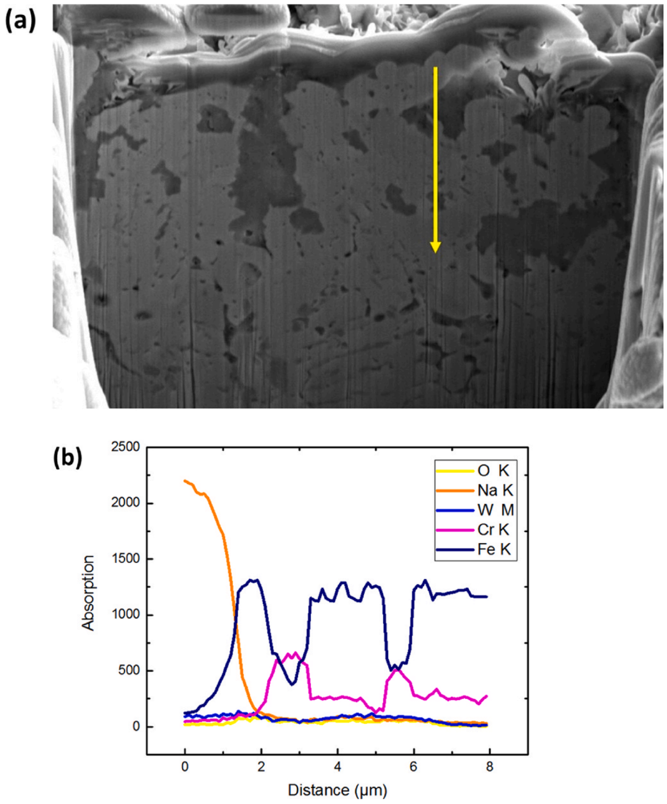

Fig. 8. FIB-SEM image of the microstructure of unirradiated Gr. 92 specimen after exposure to 650 °C sodium for 300 h: (a) SEM image and (b) EDS profiles across the interfacial region between the liquid sodium-affected metal surface and the steel substrate.

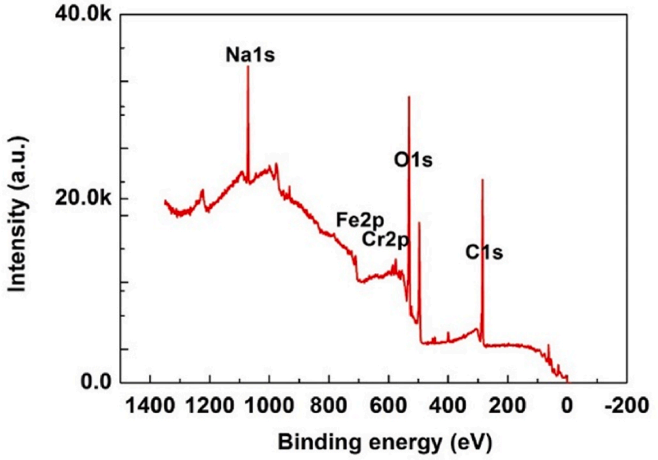

Fig. 9. XPS spectra of 1×10^{16} protons/cm^2 irradiated Gr. 92 specimen surface after 300 h exposure to 650 °C oxygen-saturated sodium modified $NaCrO_2$ compounds.

materials within liquid metal systems.

4.4. *Increasing the corrosion path*

Na_2O infiltrates the metal matrix through boundaries such as prior austenite grain boundaries and martensite lath boundaries. The $NaCrO_2$ compound is formed on the surface of the specimen, and it originates from prior austenite grain boundaries and lath boundaries, facilitating subsequent diffusion into the matrix.

The augmentation of diffusion and the amplification of corrosion potential in irradiated materials can be attributed to two factors: (1) the higher concentration of defects, such as vacancies and interstitial sites, and (2) the formation of diffusion paths like dislocation and precipitates. The diffusion of lattice atoms, facilitated by the vacancy mechanism, is described by the following:

$$D_a = f_v D_v C_v \tag{4}$$

where f_v is the correlation coefficient, D_v is the vacancy diffusion coefficient, and C_v is the vacancy concentration. Nonetheless, in the presence of radiation damage, the diffusion mechanism is governed by an augmented process whereby the diffusion of atoms within materials is

Table 2
Corrosion rate of the unirradiated specimen, 5 × 10^{15} protons/cm^2 irradiated specimen and 1 × 10^{16} protons/cm^2 irradiated specimen in oxygen-saturated liquid sodium at 650 °C for 300 h.

Specimen	Corrosion rate (mg/mm^2)		
	Unirradiated specimen	5 × 10^{15} protons/cm^2 irradiated specimen	1 × 10^{16} protons/cm^2 irradiated specimen
HT9	0.2392 ± 0.038	0.2738 ± 0.025	0.3014 ± 0.042
Gr. 92	0.2707 ± 0.047	0.3071 ± 0.023	0.3272 ± 0.036

intensified through the emergence of new pathways facilitated by defect species.

$$D_a^{irradiated} = f_v D_v C_v + f_i D_i C_i + f_{2v} D_{2v} C_{2v} + f_{2i} D_{2i} C_{2i} + \cdots \tag{5}$$

Within the context of radiation-enhanced diffusion, the equations governing defect balance yield both transient and steady-state solutions [43,44]. In the current investigation, the proton-irradiated FMS has revealed the formation of defect channels, wherein dislocations effectively clear out irradiation-induced defects within a narrow channel, thereby establishing a pathway that facilitates the easy gliding of additional dislocations.

4.5. *Irradiation hardening*

Fig. 10 shows the comparison of hardness of Gr. 92 specimen before and after proton irradiation test. A significant hardness change was observed for irradiated specimens at indentation depths. After irradiation to 5 × 10^{15} protons/cm^2 and 10^{16} protons/cm^2, the microhardness increased by 38.5 HV and 90.2 HV, respectively. The irradiation environment did not exert any influence on the hardness due to changes in grain size. The micro-indentation exhibited dimensions smaller than the grain size in both conditions.

5. Conclusions

In this study, unirradiated FMS specimens and irradiated FMS specimens were exposed to a high-temperature liquid sodium corrosive environment to investigate the consequences effects of both conditions saturated with oxygen for a duration of 300 h. At the same time, microstructural analysis was conducted to study the corrosion behavior and penetration depth. Additionally, the effects of radiation-induced precipitation on FMS due to proton irradiation were examined using comprehensive and incidence techniques. To summarize, the conclusions are as follows.

(1) The weight loss measurement showed that materials have reduced chromium content show more significant weight loss under proton irradiation.
(2) In all FMS specimens exposed to sodium, the presence of the $M_{23}C_6$ ($Cr_{23}C_6$) precipitate was observed at the interface between the Cr-depleted zone and the material matrix.
(3) Microstructural evaluation revealed the existence of chromium-rich zones beneath the surfaces of both irradiated and non-irradiated materials. Notably, the irradiated specimens exhibited chromium-rich zones with greater depths compared to the non-irradiated specimens.
(4) Proton irradiation was formed to (a) the increase of surface roughness, (b) the formation of $M_{23}C_6$, (c) the increase of dislocation and dislocation loops in steel, and (d) the formation of potential paths for corrosion by radiation defects, which are caused by irradiation.
(5) A significant hardness change was observed for irradiated specimens at indentation depths.

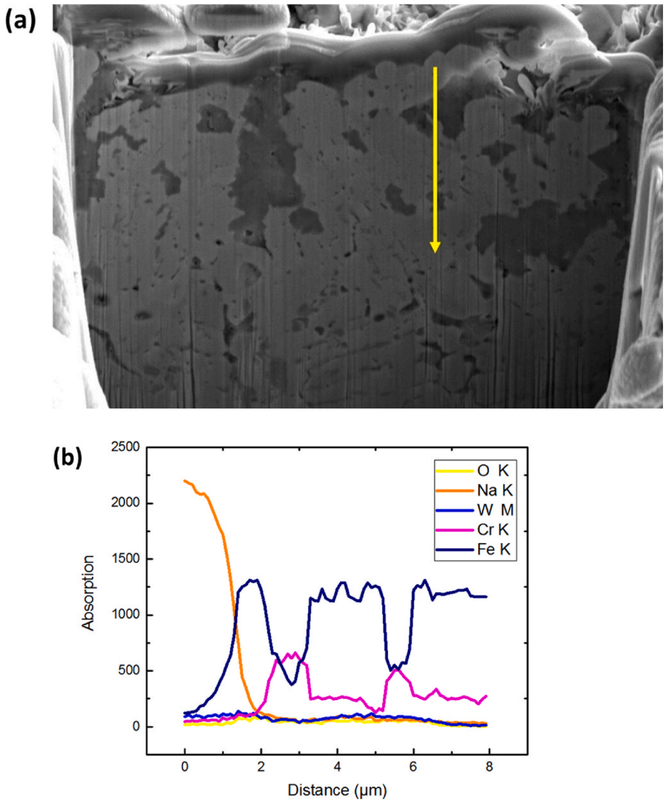

Fig. 10. Comparison of hardness of Gr.92 specimen.

Data availability

The raw/processed data required to reproduce these findings cannot be shared at this time as the data also forms part of an ongoing study.

CRediT authorship contribution statement

Jeonghyeon Lee: Writing – original draft, Methodology, Investigation. **Taeho Kim:** Writing – review & editing. **Taeyong Kim:** Writing – review & editing. **Ji Hyun Kim:** Writing – review & editing, Supervision, Conceptualization.

Declaration of competing interest

The authors declare that they have no known competing financial interests or personal relationships that could have appeared to influence the work reported in this paper.

Acknowledgements

This work was supported by the Fundamental Research Program of the Korea Institute of Materials Science (PNK 7530) and the Korea Institute of Energy Technology Evaluation and Planning of the Ministry of Trade, Industry & Energy (MOTIE) of the Republic of Korea (grant no. RS-2024-00398425).

References

[1] S.H. Shin, S.H. Kim, J.H. Kim, Model of liquid gallium corrosion with austenitic stainless steel at a high temperature, J. Nucl. Mater. 450 (2014) 314–321.
[2] K. Lambrinou, E. Charalampopoulou, T. Van der Donck, R. Delville, D. Schryvers, Dissolution corrosion of 316L austenitic stainless steels in contact with static liquid lead-bismuth eutectic (LBE) at 500 °C, J. Nucl. Mater. 490 (2017) 9–27.
[3] Sung Il Kim, Kun Jai Lee, Requirement of decontamination factor for near-surface disposal of PEACER wastes, Prog. Nucl. Energy 49 (2007) 14–19.

[4] J. Carlsson, H. Wider, Comparison of sodium and lead-cooled fast reactors regarding reactor physics aspects, severe safety and economical issues 236 (2006) 1589–1598.

[5] P. Mazgaj, P. Darnowski, S. Gurgacz, M. Lipka, K. Dziubanii, Comparison of Simple Design of Sodium and Lead Cooled Fast Reactor Cores, vol. 94, 2014, pp. 16–26.

[6] T. Evans, J. Olson, V. Bhat, S.-H. Lee, Corrosion of stainless steel battery components by bis(fluorosulfonyl)imide based ionic liquid electrolytes, J. Power Sources 269 (2014) 616–620.

[7] T. Furukawa, S. Kato, E. Yoshida, Compatibility of FBR materials with sodium, J. Nucl. Mater. 392 (2009) 249–254.

[8] S. Hun, J. Lee, J. Hwan, J. Hyun, Mechanism of corrosion of 9Cr and 12Cr ferritic/martensitic steels under oxygen-saturated sodium, Eval, Prog. Plann. 112 (2016) 611–624.

[9] D. Frazer, S. Qvist, S. Parker, D.L. Krumwiede, M. Caro, J. Tesmer, S.A. Maloy, Y. Q. Wang, P. Hosemann, Degradation of HT9 under simultaneous ion beam irradiation and liquid metal corrosion, J. Nucl. Mater. 479 (2016) 382–389.

[10] H. Yu, J. Liang, Z. Yao, M.A. Kirk, M.R. Daymond, Effect of heavy ion irradiation on thermodynamically equilibrium Zr-Excel alloy, J. Nucl. Mater. 488 (2017) 33–45.

[11] X. Huang, Y. Shen, J. Zhu, Influence of Ar-Ions Irradiation on the Oxidation Behavior of Ferritic – Martensitic Steel P92 in Supercritical Water, vol. 457, 2015, pp. 18–28.

[12] S. Teysseyre, Z. Jiao, E. West, G.S. Was, Effect of Irradiation on Stress Corrosion Cracking in Supercritical Water, vol. 371, 2007, pp. 107–117.

[13] O.K. Chopra, A.S. Rao, A review of irradiation effects on LWR core internal materials - IASCC susceptibility and crack growth rates of austenitic stainless steels, J. Nucl. Mater. 409 (2011) 235–256.

[14] Z. Jiao, G.S. Was, Impact of localized deformation on IASCC in austenitic stainless steels, J. Nucl. Mater. 408 (2011) 246–256.

[15] S.M. Bruemmer, G.S. Was, Microstructural and microchemical mechanisms controlling intergranular stress corrosion cracking in light-water-reactor, Systems 216 (1994) 348–363.

[16] P. Ahmedabadi, V. Kain, K. Arora, I. Samajdar, S.C. Sharma, P. Bhagwat, Radiation-induced Segregation in Desensitized Type 304 Austenitic Stainless Steel, vol. 416, 2011, pp. 335–344.

[17] G.S. Was, J.P. Wharry, B. Frisbie, B.D. Wirth, D. Morgan, J.D. Tucker, T.R. Allen, Assessment of Radiation-Induced Segregation Mechanisms in Austenitic and Ferritic – Martensitic Alloys, vol. 411, 2011, pp. 41–50.

[18] S.H. Shin, J.H. Kim, J.H. Kim, Corrosion behavior and microstructural evolution of ASTM A182 Grade 92 steel in liquid sodium at 650 °C, Corrosion Sci. 97 (2015) 172–182.

[19] A. Sarkar, A. Kumar, S. Mukherjee, S.K. Sharma, D. Dutta, P.K. Pujari, A. Agarwal, S.K. Gupta, P. Singh, J.K. Chakravartty, Investigation of microstructure and mechanical properties of proton irradiated Zircaloy 2, J. Nucl. Mater. 479 (2016) 524–532.

[20] Q. Xu, K. Fukumoto, Y. Ishi, Y. Kuriyama, T. Uesugi, K. Sato, Y. Mori, T. Yoshiie, Irradiation damage from low-dose high-energy protons on mechanical properties and positron annihilation lifetimes of Fe–9Cr alloy, J. Nucl. Mater. (2015) 88–91.

[21] N.Q. Lam, G.K. Leaf, Mechanisms and Kinetics of Ion Implantation, vol. 60439, 2016, pp. 251–267.

[22] P. Ahmedabadi, V. Kain, K. Arora, I. Samajdar, S.C. Sharma, P. Bhagwat, Radiation-induced segregation in desensitized type 304 austenitic stainless steel, J. Nucl. Mater. 416 (2011) 335–344.

[23] J. Lee, S.H. Shin, J.K. Lee, S. Choi, J.H. Kim, Corrosion behavior of surface treated steel in liquid sodium negative electrode of liquid metal battery, J. Power Sources 307 (2016) 526–537.

[24] O. Yeliseyeva, V. Tsisar, G. Benamati, Influence of temperature on the interaction mode of T91 and AISI 316L steels with Pb–Bi melt saturated by oxygen, Corrosion Sci. 50 (2008) 1672–1683.

[25] Z. Jiao, G.S. Was, Precipitate evolution in ion-irradiated HCM12A, J. Nucl. Mater. 425 (2012) 105–111.

[26] Z. Jiao, V. Shankar, G.S. Was, Phase stability in proton and heavy ion irradiated ferritic-martensitic alloys, J. Nucl. Mater. 419 (2011) 52–62.

[27] J. He, F. Wan, K. Sridharan, T.R. Allen, A. Certain, Y.Q. Wu, Response of 9Cr-ODS steel to proton irradiation at 400 ??c, J. Nucl. Mater. 452 (2014) 87–94.

[28] S.H. Shin, J.J. Kim, J.A. Jung, K.J. Choi, I.C. Bang, J.H. Kim, A study on corrosion behavior of austenitic stainless steel in liquid metals at high temperature, J. Nucl. Mater. 422 (2012) 92–102.

[29] S.H. Shin, J.H. Lee, J.K. Lee, J.H. Kim, Correlation between carbon activity and carbon content in α-iron in liquid sodium negative electrode of liquid metal battery, J. Power Sources 297 (2015) 105–112.

[30] S. Hémery, T. Auger, J.L. Courouau, F. Balbaud-Célérier, Effect of oxygen on liquid sodium embrittlement of T91 martensitic steel, Corrosion Sci. 76 (2013) 441–452.

[31] G.T. Burstein, P.C. Pistorius, Surface Roughness and the Metastable Pitting of Stainless Steel in Chloride Solutions, 1995.

[32] T. Hong, M. Nagumo, Effect of surface roughness on early stages of pitting corrosion of type 301 stainless steel, Corrosion Sci. 39 (1997) 1665–1672.

[33] K. Sasaki, G.T. Burstein, The generation of surface roughness during slurry erosion-corrosion and its effect on the pitting potential, Corrosion Sci. 38 (1996) 2111–2120.

[34] G.T. Burstein, S.P. Vines, Repetitive nucleation of corrosion pits on stainless steel and the effects of surface roughness, J. Electrochem. Soc. 148 (2001) 504–516.

[35] G. Gupta, Z. Jiao, A.N. Ham, J.T. Busby, G.S. Was, Microstructural evolution of proton irradiated T91, J. Nucl. Mater. 351 (2006) 162–173.

[36] W. Kesternich, R. V Nandedkar, Coprecipitation of $M_{23}C_6$, and MC type carbide under the influence of irradiation, J. Nucl. Mater. 179–181 (2) (1991) 1015–1018.

[37] P.P. Liu, R. Yu, Y.M. Zhu, M.Z. Zhao, J.W. Bai, F.R. Wan, Q. Zhan, Deuterium ion irradiation induced precipitation in Fe – Cr alloy : characterization and effects on irradiation behavior, J. Nucl. Mater. 459 (2015) 81–89.

[38] T. Suzuki, I. Mutoh, Compatibility of high-purity Fe-(5 to 15)Cr-1Mo ferritic steels in a sodium environment, J. Nucl. Mater. 149 (1987) 41–50.

[39] J.H. Kim, S.H. Kim, Microstructure and mechanical property of ferritic-martensitic steel cladding under a 650 C liquid sodium environment, J. Nucl. Mater. 443 (2013) 112–119.

[40] P. Dubuisson, D. Gilbon, D.T.A.C. Dtm, S. De Recherches, M. Appliqukes, C. E. Saclay, Microstructural evolution of ferritic-martensitic irradiated in the fast breeder reactor Phénix, J. Nucl. Mater. 205 (1993) 178–189.

[41] P.J. Maziasz, Formation and stability of radiation-induced phases in neutron-irradiated austenitic and ferritic steels, J. Nucl. Mater. 169 (2008) 95–115.

[42] Y. Chen, Irradiation effects of ht-9 martensitic steel, Nucl. Eng. Technol. 45 (2013) 311–322.

[43] R. Sizmann, The effect of radiation upon diffusion in metals, J. Nucl. Mater. 70 (1978) 386–412.

[44] J.P. Wharry, G.S. Was, ScienceDirect the mechanism of radiation-induced segregation in ferritic–martensitic alloys, Acta Mater. 65 (2014) 42–55.